29th Symposium on Naval Hydrodynamics
Gothenburg, Sweden, 26-31 August 2012

Large Eddy Simulation of Crashback in Ducted Propellers with Stator Blades

Hyunchul Jang[1] and Krishnan Mahesh[1]
([1]Aerospace Engineering & Mechanics, University of Minnesota, USA.)

ABSTRACT

Crashback is an off-design operating condition where a propeller rotates in the reverse direction to yield negative thrust. Large Eddy Simulation (LES) for the crashback in an open propeller was validated against Jessup *et al.* (2004)'s experiments and showed good agreement by Jang & Mahesh (2012). In this paper, a sliding interface method is developed to enable a simulation of the rotor-stator problem, and the effect of a duct with stator blades in crashback is studied using LES in relatively rotating grid systems performed by the sliding interface method. Computed unsteady loads show good agreement with the experimental results. Thrust mostly arises from the blade surface, but most of side-force is generated from the duct surface. The side-force on the ducted propeller is caused by the blade-duct interaction. Strong tip leakage flow is observed behind the suction side at the tip gap. The physical source of the tip leakage flow is seen to be the large pressure difference between pressure and suction sides.

INTRODUCTION

When a marine vessel is quickly decelerated, the propeller of the vehicle is forced to rotate in the reverse direction. This off-design operating condition of the forward vessel velocity and the reverse propeller rotation is termed crashback. Flow around the propeller in crashback is characterized by large scale unsteadiness and separation. Thus, the crashback condition is one of the most complex and challenging conditions to analyze. Low frequency and high amplitude off-axis forces and moments generated by the unsteadiness can cause severe loss of maneuverability of the vessel and have the potential impairment of the propeller blades. The prominent feature of crashback is a highly unsteady vortex ring structure, which is created by interaction of the free stream flow with the strong reverse flow from reverse propeller rotation.

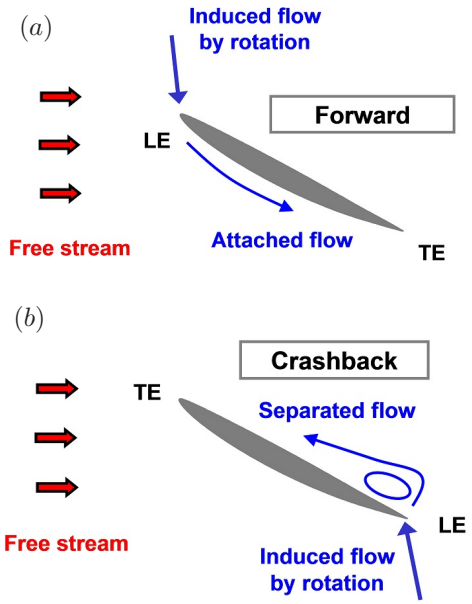

Figure 1: Schematic of flow around the radial cross-section of a blade: (a) in forward condition, (b) in crashback condition. (Jang & Mahesh, 2012)

In the crashback condition, the leading and trailing edges of propeller blades exchange their roles as compared to the design condition termed the forward condition. Figure 1 illustrates flow around the cross-section of the blade in forward and crashback conditions. The flow at the smooth leading edge (LE) is mostly attached in the forward condition, but large flow separation could occur at the sharp LE in the crashback. The large flow separation can cause high amplitude unsteady fluctuations in blade loads. Large Eddy Simulation (LES) is therefore used to predict the fluctuating loads.

Crashback has been studied for open propellers experimentally and computationally. The first crashback experiments were conducted by Hecker & Remmers (1971) in open water. Thrust and torque coef-

ficients were measured for several propellers in their experiments. Jiang *et al.* (1997) studied the evolution of the unsteady vortex ring using Particle Image Velocimetry (PIV) for propeller P4381 in water tunnel (WT). Jessup *et al.* (2004) presented more detailed measurements of flow around the same propeller using PIV and Laser Doppler Velocimetry (LDV). Bridges *et al.* (2008)'s experiment reported the effect of upstream hull on the open propeller.

Chen & Stern (1999) performed simulations of the flow around the open propeller using unsteady Reynolds-Averaged Navier-Stokes (RANS) equations. These studies showed that RANS yielded good results for forward condition but produced significant disparities in crashback condition. Vyšohlid & Mahesh (2006, 2007) performed LES for the propeller at an advance ratio of $J = -0.7$ and showed good agreement for mean and RMS of unsteady loads as well as spectra. Chang *et al.* (2008) performed LES at other advance ratios, $J = -0.5$ and $J = -1.0$ and demonstrated the fluid-structure-interaction capability of LES with a finite-element structural solver. Jang & Mahesh (2010, 2012) introduced pressure contributions to unsteady loads in order to understand the origin of thrust and side-force and used conditional averaging to study extreme amplitude events. Verma *et al.* (2011, 2012) performed LES for the open propeller with an upstream submarine hull.

The effect of a duct in crashback was experimentally studied by Jessup *et al.* (2006) and Donnelly *et al.* (2008). The addition of a duct tended to move the ring vortex outboard and maintained attached flow on the outer duct surface. Jang & Mahesh (2008) investigated the effect of the duct in crashback for the same propeller using LES. However, stator blades originally installed in the experiment were ignored in the computation for solving the problem in a rotating frame of reference. As a result, the computed unsteady loads showed significant discrepancy from experimental results.

The objective of the present paper is to: (i) develop a sliding interface method on massively parallel computing platform and validate the method, (ii) understand flow physics of crashback in ducted propellers with stator blades.

SIMULATION DETAILS

Numerical Method

The sliding interface method is used to handle relatively rotating grid systems. Relatively rotating grids do not have to overlap since the movement of the grid

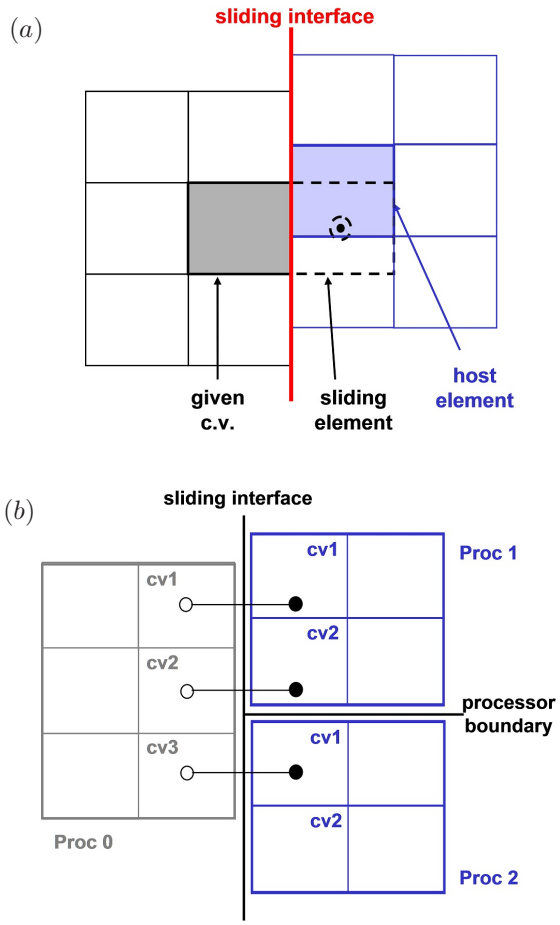

Figure 2: Schematic for the sliding interface method: (a) without consideration of multiple processors, (b) with consideration of multiple processors.

is a rigid rotation. The only intersection is an interface between the grids, which is called the sliding interface. Data exchange between the grids can be performed only at the sliding interface so that no remeshing, deformation, or hole cutting is required. The sliding interface method has been used by several researchers on multi-block structured grids (MacPherson *et al.*, 2006; Steijl & Barakos, 2008) and on unstructured grids (Pan *et al.*, 2001; Blades & Marcum, 2007).

The sliding interface method developed for this study is capable of being applied on arbitrarily shaped unstructured grids on massively parallel computing platforms. Figure 2 shows a schematic for the sliding interface method on an unstructured grid. Sliding elements of a sub-domain are created by extrusion to the adjacent sub-domain. However, sliding elements of the sub-domain and boundary cells of the

adjacent sub-domain do not match due to the relative rotation between the sub-domains. As shown in figure 2(a), a sliding element (black dashed) is extruded from a boundary control volume (black shaded) in the left sub-domain. Since the grids of the two sub-domains do not align, the control volume containing the sliding element is not known without a search process. The control volume is named the host element and shaded in blue.

The sliding interface method is being developed for parallel computation. Thus, the processor block which contains the sliding element also must be found. The processor block is called the host processor hereafter. Figure 2(b) explains the host element and the host processor at the multiple processor boundaries with the sliding interface. The sliding element corresponding to '$cv1$' of '$proc0$' is located in '$cv1$' of '$proc1$'. The host processor of the sliding element is '$proc1$', and the host element is '$cv1$' in the host processor. Three central issues need to be addressed; search algorithm in multiple processors, efficient data structure for the message passing, and the interpolation scheme at the sliding element.

The governing equations for the sliding interface method are expressed in the Arbitrary Eulerian-Lagrangian (ALE) formulation (Donea *et al.*, 2004). In LES, large scales are directly solved from the spatially filtered Navier-Stokes (N-S) equations, while small scales are accounted for by modeling the subgrid stress. The filtered N-S equations in the ALE formulation are as follows:

$$\begin{aligned} \frac{\partial \bar{u}_i}{\partial t} + \frac{\partial}{\partial x_j}(\bar{u}_i\bar{u}_j - \bar{u}_i V_j) &= -\frac{\partial \bar{p}}{\partial x_i} \\ &+ \nu\frac{\partial^2 \bar{u}_i}{\partial x_j \partial x_j} - \frac{\partial \tau_{ij}}{\partial x_j}, \\ \frac{\partial \bar{u}_i}{\partial x_i} &= 0, \end{aligned} \tag{1}$$

where u_i is the Cartesian velocity, p is the pressure, ν is the kinematic viscosity, V_j is the grid velocity, the overbar denotes the spatial filter, and $\tau_{ij} = \overline{u_i u_j} - \bar{u}_i\bar{u}_j$ is the sub-grid stress. The dynamic Smagorinsky model proposed by Germano *et al.* (1991) and modified by Lilly (1992) is used to model the subgrid stress in the paper. The grid velocity is given by $V_j = \epsilon_{jkl}\omega_k x_l$ in this study due to the rigid rotation of the grid where ω_j is the angular velocity of the rotating sub-domain and ϵ_{ijk} denotes the permutation symbol. Since there is no mesh deformation, the geometric conservation law is automatically satisfied so that no spurious mass sources or sinks are created.

Equation (2) is solved using a numerical method developed by Mahesh *et al.* (2004) for incompressible flows on unstructured grids. The algorithm is derived to be robust without numerical dissipation. It is a finite-volume approach which stores the Cartesian velocities and the pressure at the centroids of the cells, and the face normal velocities are stored independently at the centroids of the faces. A predictor-corrector approach is used. The predicted velocities at the control volume centroids are first obtained and then interpolated to obtain the face-normal velocities. The predicted face normal velocity is projected so that the continuity equation is discretely satisfied. This yields a Poisson equation for pressure which is solved iteratively using a algebraic multi-grid method. The pressure field is used to update the Cartesian velocities using a least-squared approach for minimizing the conservation error. Implicit time advancement is performed using the Crank-Nicholson scheme. The algorithm has been validated for a variety of problems over a range of Reynolds numbers (Mahesh *et al.*, 2004).

Problem Description

The simulations are performed for marine propeller P4381, which is five-bladed, right-handed with variable pitch, has no skew and no rake. The propeller has been used in various experiments (Jiang *et al.*, 1997; Jessup *et al.*, 2004, 2006) and computations (Chen & Stern, 1999; Vyšohlid & Mahesh, 2006; Chang *et al.*, 2008; Jang & Mahesh, 2012; Verma *et al.*, 2012).

Simulations are performed in crashback at a negative advance ratio of $J = -0.7$ and Reynolds number of $Re = 480,000$. The advance ratio J and Reynolds number Re are defined as

$$J = \frac{U}{nD}, \qquad Re = \frac{DU}{\nu} \tag{2}$$

where U is the free-stream velocity, D is the diameter of the propeller disk, n is the rotational speed, and ν is the kinematic viscosity.

The thrust T is defined as the axial component of the force, and torque Q is the axial component of moment of the force. F_H and F_V denote horizontal and vertical components of the force whose vector sum yields side-force S. Non-dimensional thrust coefficient K_T, torque coefficient K_Q, and side-force coefficient K_S are defined as:

$$\begin{aligned} K_T = \frac{T}{\rho n^2 D^4}, \quad K_Q = \frac{Q}{\rho n^2 D^5}, \\ K_S = \frac{\sqrt{{F_H}^2 + {F_V}^2}}{\rho n^2 D^4}, \end{aligned} \tag{3}$$

where a rotational velocity nD is used as the reference velocity, and D^2 is used as the reference area in this normalization. Hereafter, $\langle K \rangle$ denotes mean value, and $\sigma(K)$ denotes standard deviation.

The present simulation is compared to Jessup *et al.* (2004, 2006)'s experiments. They performed 36 inch water tunnel (WT) experiments for both open and ducted propellers. The WT experiments measured time series of unsteady loads and two-dimensional flow fields from LDV measurement, but they might have the tunnel confinement effect because the tunnel diameter was only three times larger than the propeller diameter except for the test section. Open water (OW) experiment does not have the tunnel effect, but limited data can be obtained. Thus, both WT and OW results are compared to the computation results.

CRASHBACK IN OPEN PROPELLER

Validation of LES

The current LES methodology has been validated for an open propeller in crashback at $J = -0.7$ by Jang & Mahesh (2012). Their computation showed good agreement with the experimental results of Jessup *et al.* (2004, 2006). Computed mean values of K_T and K_Q were between the WT and OW results as shown in table 1. The agreement with experimental data was within the scatter observed between the experiments. Similarly, standard deviations and side-force magnitude showed good agreement with the WT experiment.

Figure 3 compares profiles from computed time averaged flow fields to those from the LDV measurements of Jessup *et al.* (2004, 2006). Profiles are extracted from five $x-$locations two upstream of the propeller (x/R=-0.39 and -0.25), and three downstream of the propeller (x/R=0.25, 0.50, and 0.75). All the profiles (axial, radial, tangential velocities, and turbulent kinetic energy) from the LES agree well with the experiment.

Validation of Sliding Interface Method

The validity of the sliding interface method is verified by comparison to the rotating reference frame approach. The computational domain for the sliding interface method is split into two sub-domains; one containing the rotor blades is set to the rotating sub-domain and the other is the stationary sub-domain. The 8 million grid is created in exactly the same manner except for the existence of the sliding interface. Both sub-domains are individually partitioned for the sliding interface method by the *METIS* library

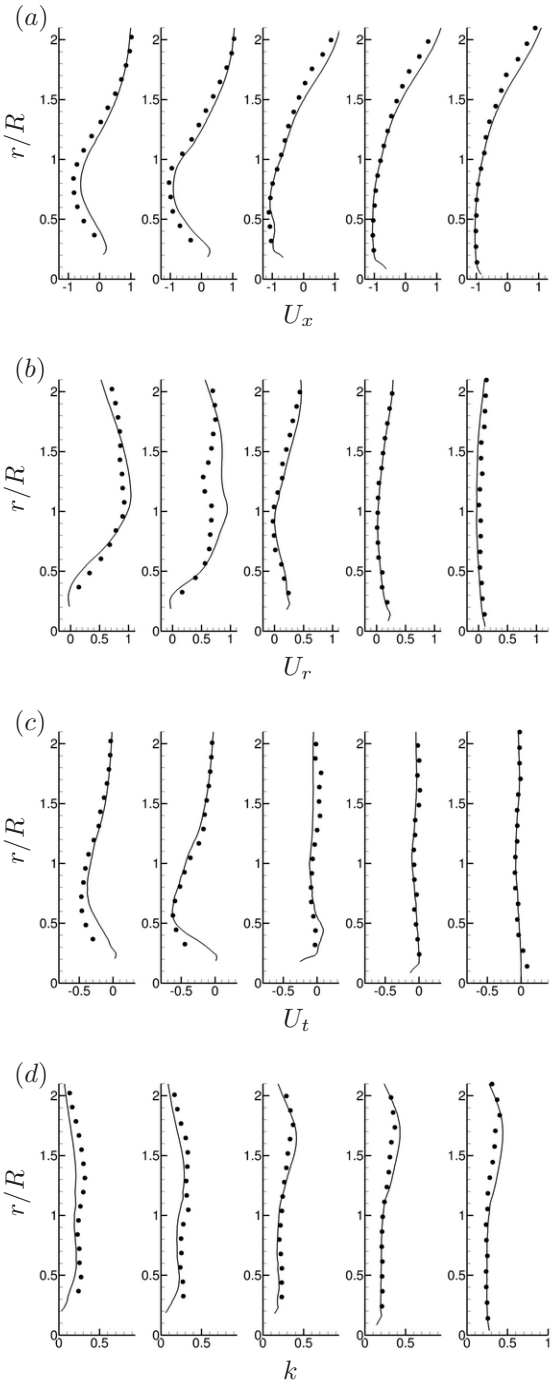

Figure 3: Profiles from time averaged flow field for open propeller: (a) axial velocity, (b) radial velocity, (c) tangential velocity, (d) turbulent kinetic energy. Locations of profiles are x/R=-0.39, x/R=-0.25, x/R=0.25, x/R=0.50, and x/R=0.75, respectively (—— LES , • WT). (Jang & Mahesh, 2012)

	$\langle K_T \rangle$	$\sigma(K_T)$	$\langle K_Q \rangle$	$\sigma(K_Q)$	$\langle K_S \rangle$
LES	-0.38	0.055	-0.074	0.010	0.027
WT	-0.33	0.060	-0.065	0.011	0.030
OW	-0.41	·	-0.078	·	·

Table 1: Statistics of unsteady loads for open propeller. (Jang & Mahesh, 2012)

(Karypis & Kumar, 1998). Figure 4 compares processor boundaries in $x-y$ plane with pressure contours from two approaches: the rotating reference frame approach and the sliding interface method. The processor boundaries are denoted by the black solid lines. The sliding interface is emphasized by an ellipse in figure 4(b). The pressure contour across the sliding interface looks good, i.e. no jump of the pressure is observed across the sliding interface.

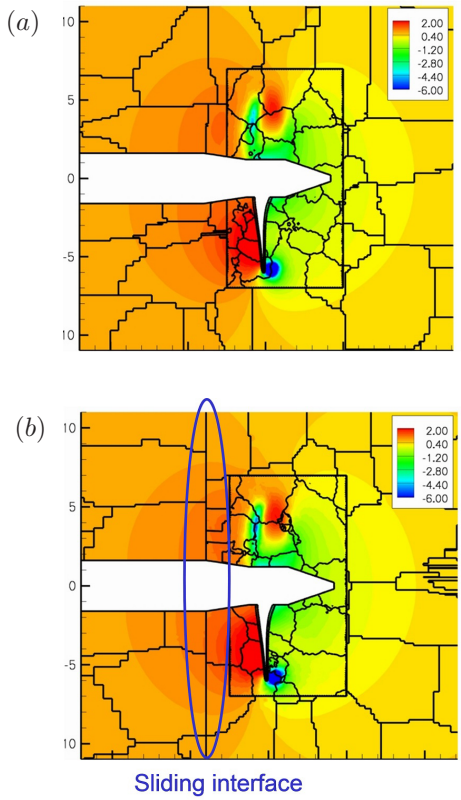

Figure 4: Comparison of processor boundaries with pressure contours from two approaches: (a) the rotating reference frame approach, (b) the sliding interface method.

Instantaneous flow fields from the sliding interface method are compared to those from the rotating reference frame approach at the same time in figure 5. The instantaneous flow fields are given at Re=60,000 and 3.0 *revs*. Pressure contours from those approaches show almost the same results in figure 5(a) and (b). The axial velocities in figure 5(c) and (d) also look similar. Time histories of K_T from both approaches are compared in figure 6, and show reasonable agreement.

CRASHBACK IN DUCTED PROPELLER WITH STATOR BLADES

To investigate the effect of a duct on crashback, a neutrally loaded duct was added around the propeller in Jessup *et al.* (2006). The hub geometry of the ducted propeller was slightly modified from that of the open propeller for installation of measuring devices. The designed ducted propeller also had 13 stator blades upstream of rotor blades as shown in figure 7(a). However, the ducted propeller with stator blades cannot be solved in a rotating frame of reference since the stator blades are not axi-symmetric. Thus, the previous work of Jang & Mahesh (2008) was performed in the rotating frame without consideration of the stator blades. Even though the stator blades are designed to contribute no additional loading at the design advance ratio, their performance in crashback is unknown. In this paper, the the sliding interface method is used to simulate the ducted propeller with stator blades.

Computational Domain and Grid

The computational domain is a cylinder with the diameter of $7.0D$ and the length of $14.0D$. Freestream velocity boundary conditions are specified at the inlet and the lateral boundaries. Convective boundary conditions are prescribed at the exit. No slip boundary conditions are specified on solid walls, but those on the rotor parts are $\vec{U} = \vec{r} \times \vec{\omega}$ since the no slip condition on the rotor parts should be considered in the rotating grid. A schematic of the computational domain and boundary conditions is shown in figure 7(b).

Figure 8(a) shows the computational grid for the ducted propeller with the stator blades. In the figure, the red colored line represents the sliding interface, and the left sub-domain is the stationary grid, and

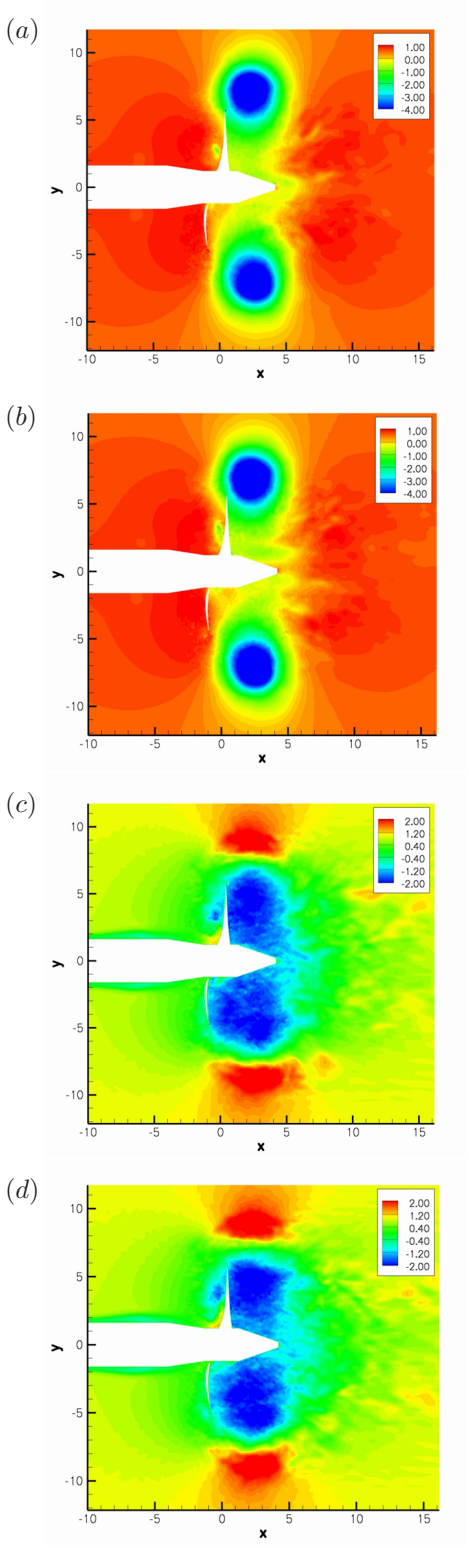

Figure 5: Comparison of instantaneous flow fields from two approaches: (a) pressure in the rotating reference frame, (b) pressure from the sliding interface method, (c) axial velocity in the rotating reference frame, (d) axial velocity from the sliding interface method.

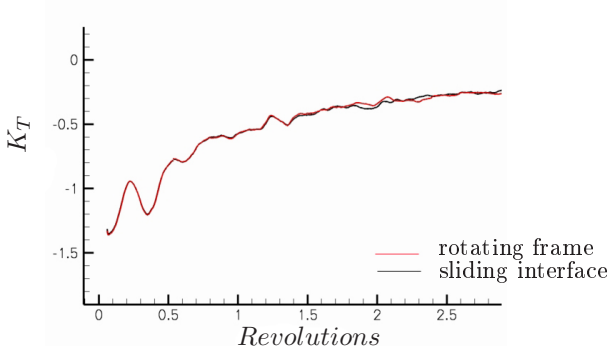

Figure 6: Comparison of K_T from two approaches.

the right sub-domain is the rotating grid. A closer look in figure 8(b) clearly shows that meshes and even processor boundaries are not matched at the sliding interface. Tetrahedral elements are used to match the complex geometry of the propeller such as rotor, stator, and duct surfaces, and the outer region consists of hexahedral elements. Four prism layers are extruded from solid walls in order to improve the wall resolution with the first height of $6.67 \times 10^{-4} D$ and growth rate of 1.05. Hexahedral elements are also used near the sliding interface to obtain better accuracy from the interpolation at the non-matching boundary. The total number of the computational c.v.'s is approximately 27 million.

Time History of Unsteady Loads

The simulation with the sliding interface method is performed for the ducted propeller with stator blades until 34.7 *revs*, and statistics of the unsteady loads are computed over 18.9 *revs*. Time histories of K_T, K_Q, and K_S are plotted in figure 9. Black solid, blue dashed, and red dotted lines represent unsteady loads on blade, duct, stator surfaces, respectively. Even though the number of revolutions does not seem to be long enough as compared to the open propeller case, the time histories show that usual transients are absent. However, longer computation is necessary to ensure that the time series are converged. In the figure, the effect of the duct on thrust is relatively small and that on torque is negligible, but the duct surface is the primary contributor to side-force. The stator effect on thrust is very small, but is significant on torque.

Mean values of unsteady loads from the computation and the WT experiments are enumerated in tables 2 and 3, respectively. Duct forces were not measured in Jessup *et al.* (2006)'s experiment, and Donnelly *et al.* (2008) measured the side-force magnitude on the duct surface. Thus, loads on the blade

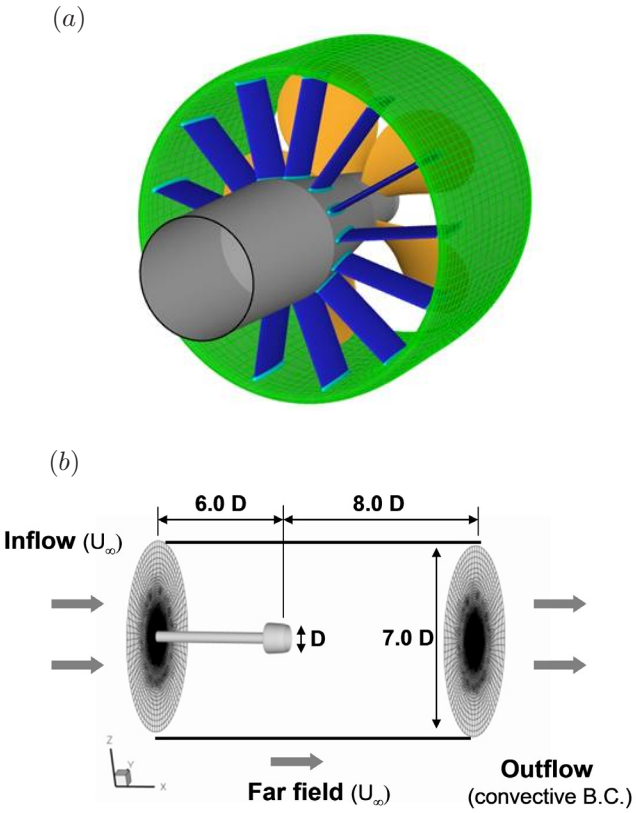

Figure 7: (a) Geometry of ducted propeller with stator blades, (b) computational domain and boundary conditions.

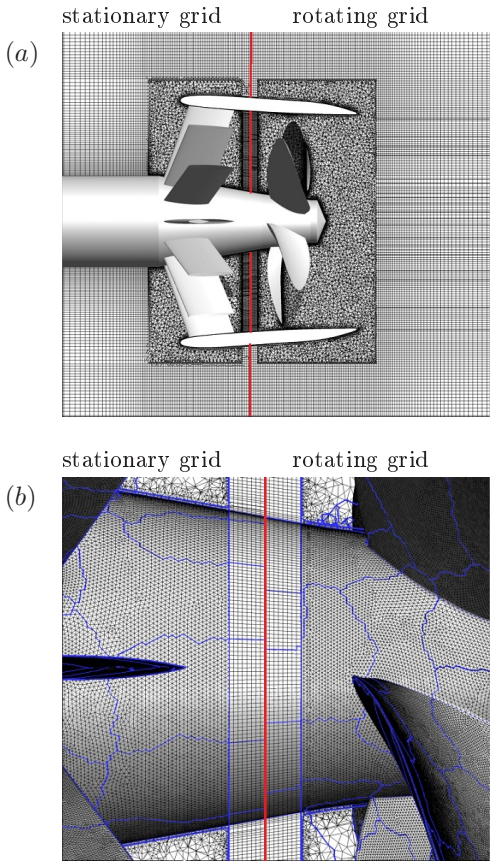

Figure 8: Computational grid for ducted propeller with stator blades; (a) in $x-y$ plane, (b) closer look at the grid. The red line represents the sliding interface and blue lines denote the processor boundaries.

surface are compared to Jessup *et al.* (2006)'s experiment, and those on the duct surface are compared to Donnelly *et al.* (2008). Even though the number of revolutions is not long enough, the computed results show reasonable agreement with experimental results. Especially, thrust and torque are almost the same as the experimental results. Since the stator blades are attached on the duct surface, the duct force can be considered as the sum of loads on duct and stator blades. $\langle K_S \rangle$ computed on the duct and stator surfaces are in favorable agreement. In sum, the effect of the duct on thrust is relatively small, and that on the torque is significantly large. Also, side-force is mainly generated from the duct surface.

Flow Field

Instantaneous flow fields for the ducted propeller with stator blades are shown in figure 10. The highly unsteady flow interaction is observed, and pressure contours are smoothly connected at the sliding interface in figure 10(a). The pressure distribution is plotted in figure 10(b). High pressure regions are observed at the leading edge of the stator blades near the inner surface of the duct. Three dimensional complexity of the vortex ring in crashback is clearly shown in figure 10(c) by using iso-contour of a constant low pressure. The duct surface is not plotted to show flow feature without obstruction of the duct in figure 10(b) & (c).

Figure 11 compares circumferentially averaged flow fields for ducted and open propeller. The blanked out zone is located where blades, shaft, stators, and duct pass through during the rotation. Axial velocity contours with streamlines are plotted in figures 11(a) and 11(b). The strong reverse flow is observed at the inflow of the propeller in both open and ducted propellers, but the reverse flow is also strong along the inner surface of the duct. Note that the strong forward velocity is observed at the gap between the blade tip and the duct, which represents the tip leakage flow. The flow on the outer surface of the duct is almost at-

	$\langle K_T \rangle$	$\langle K_Q \rangle$	$\langle K_S \rangle$
LES (blade)	-0.40	-0.078	0.023
LES (duct)	-0.069	0.00037	0.071
LES (stator)	0.0060	0.050	0.016
LES (duct+stator)	-0.063	0.050	0.087

Table 2: Unsteady loads for ducted propeller with stator blades from computation.

	$\langle K_T \rangle$	$\langle K_Q \rangle$	$\langle K_S \rangle$
WT (blade)	-0.38	-0.078	0.024
WT (duct)	·	·	0.098

Table 3: Unsteady loads for ducted propeller from WT experiment.

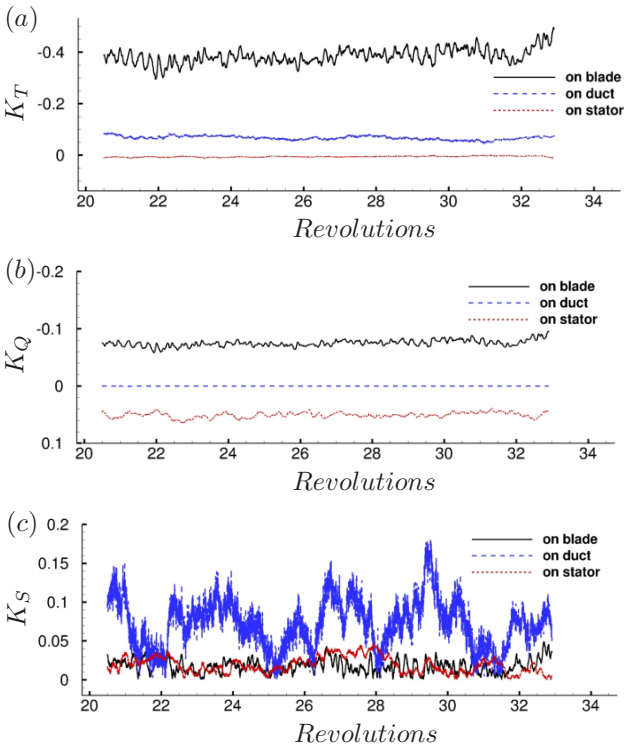

Figure 9: Time histories of unsteady loads on the ducted propeller with stators blades: (a) K_T, (b) K_Q, (c) K_S.

tached and the vortex ring core moves more outboard with the duct. Figures 11(c) and 11(d) show pressure contours for ducted and open propellers. The pressure difference between pressure and suction sides are much higher for the ducted propeller. A high pressure region is located near the tip gap of the duct, and the large pressure difference at the tip gap causes the strong tip leakage flow.

To investigate where the majority of the side force is generated on the duct, contours of RMS pressure are plotted on the duct surface in figure 12(a) & (b). The duct surface is divided into inner surface and outer surfaces and unfolded on the $x-\theta$ plane. The slanted lines in figures 12(a) represent locations of the blade tips. Note that the levels of RMS pressure on the inner surface are much higher than those on the outer surface, especially in the vicinity of blade tips. This behavior indicates that the side force on duct mostly originates from blade-duct interaction. Axial velocity on the inner surface of the duct is plotted in figure 12(c). Forward velocity near the blade tip is related to the tip leakage flow. Reverse flow are observed along the top surface of stator blades. We call the top surfaces the pressure side of the stator blades and the bottom surface the suction side.

Time averaged flow fields are shown on stator blades in figure 13. The axial velocity is almost reverse on pressure side, and the reverse flow is the strongest along the duct surface in figure 13(b). However, the reverse flow induced by the propeller rotation and the free stream flow interact on the suction side in figure 13(a). The effective pressure introduced in Jang & Mahesh (2010, 2012) is applied on the stator blades to understand the local contribution of stator blade surface to thrust and side-force. The effective pressure for thrust $\langle T \rangle$ and side-force $\sqrt{\langle S^2 \rangle}$ are defined as follows;

$$\langle T \rangle = \langle p \rangle (\vec{n}_f \cdot \vec{i}), \quad (4)$$

$$\sqrt{\langle S^2 \rangle} = \sigma(p) \sqrt{(\vec{n}_f \cdot \vec{j})^2 + (\vec{n}_f \cdot \vec{k})^2}, \quad (5)$$

where p is the pressure, $\vec{n}_f$ is the outward normal vector of a face, and $\vec{i}, \vec{j}, \vec{k}$ are base unit vectors. The positive thrust is mostly generated along the upper part of leading edge on the pressure side in figure 13(c), and the negative thrust is generated along the lower part of leading edge on both sides. This radial distribution of the effective pressure for thrust can account for the significantly large torque on stator blades even though thrust is negligibly small in table

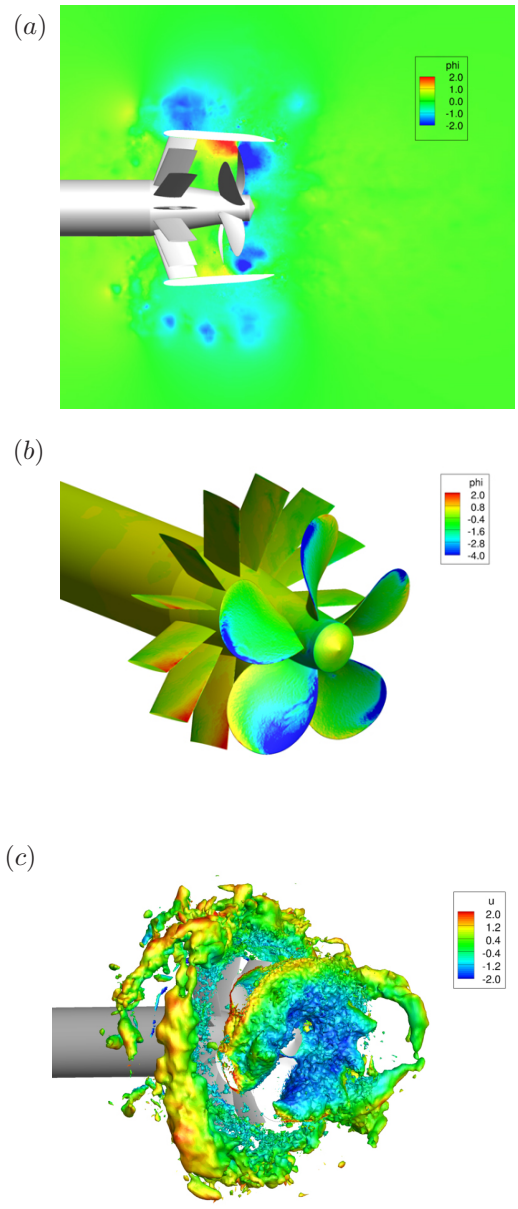

Figure 10: Instantaneous flow fields over ducted propeller with stator blades: (a) pressure in $x-y$ plane, (b) pressure on propeller surface, (c) iso-contour of pressure ($C_p = -1$) colored by axial velocity.

2. The side-force is created along the upper part of leading edge on the suction side in figure 13(e).

CRASHBACK IN DUCTED PROPELLER WITHOUT STATOR BLADES

Simulation for ducted propeller without stator blades is also performed to study the effect of stator

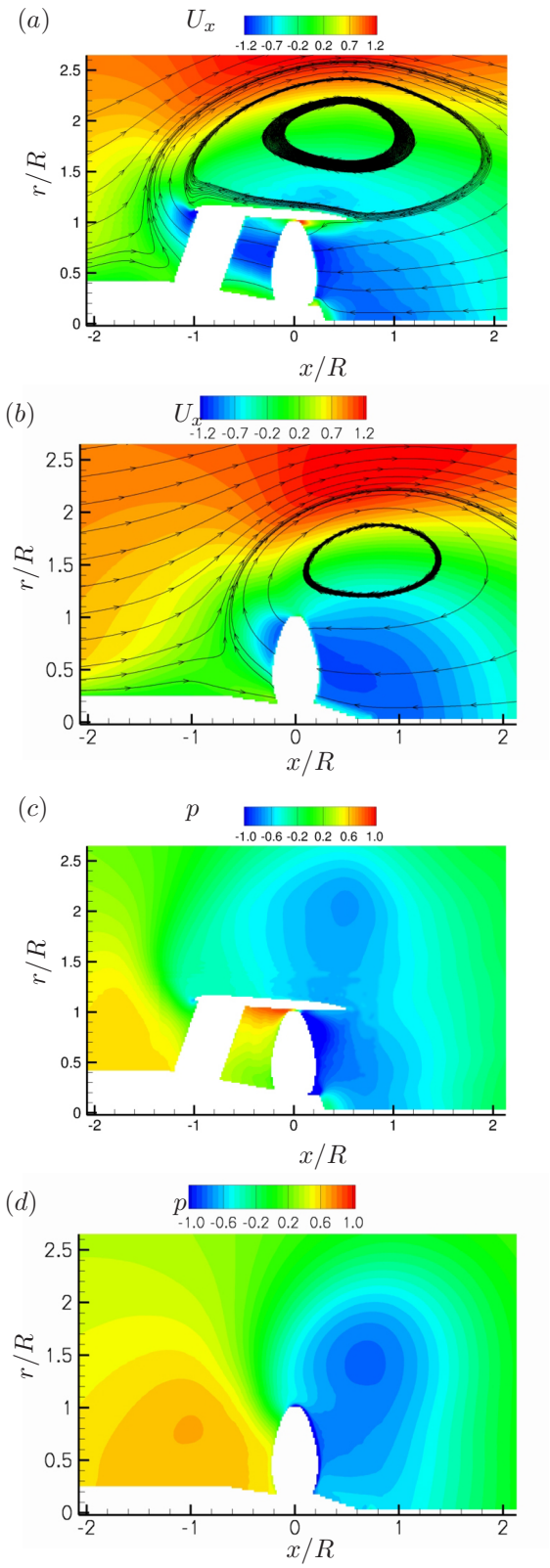

Figure 11: Circumferentially averaged averaged flow fields for open and ducted propeller: (a) axial velocity with streamlines (ducted), (b) axial velocity with streamlines (open), (c) pressure (ducted), (d) pressure (open).

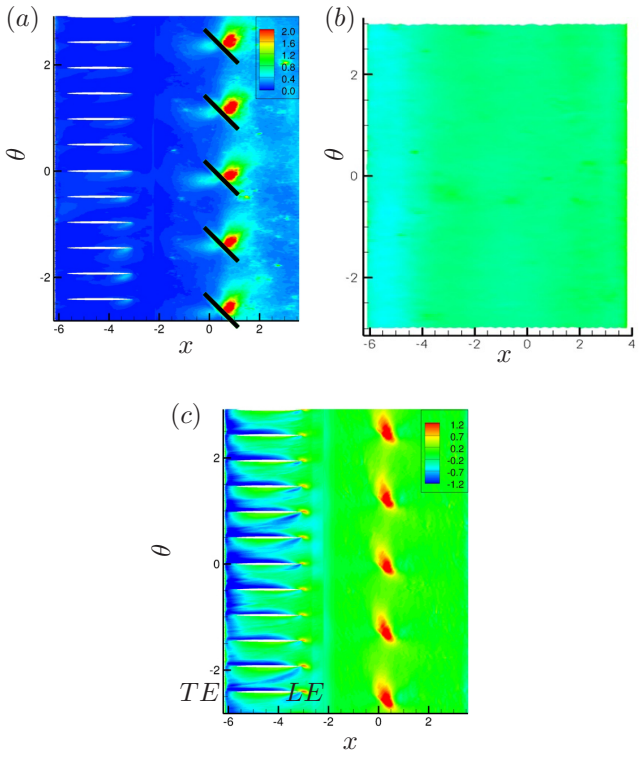

Figure 12: Time averaged flow fields on the duct surface: (a) $\sigma(p)$ on the inner surface, (b) $\sigma(p)$ on the outer surface, (c) axial velocity on the inner surface.

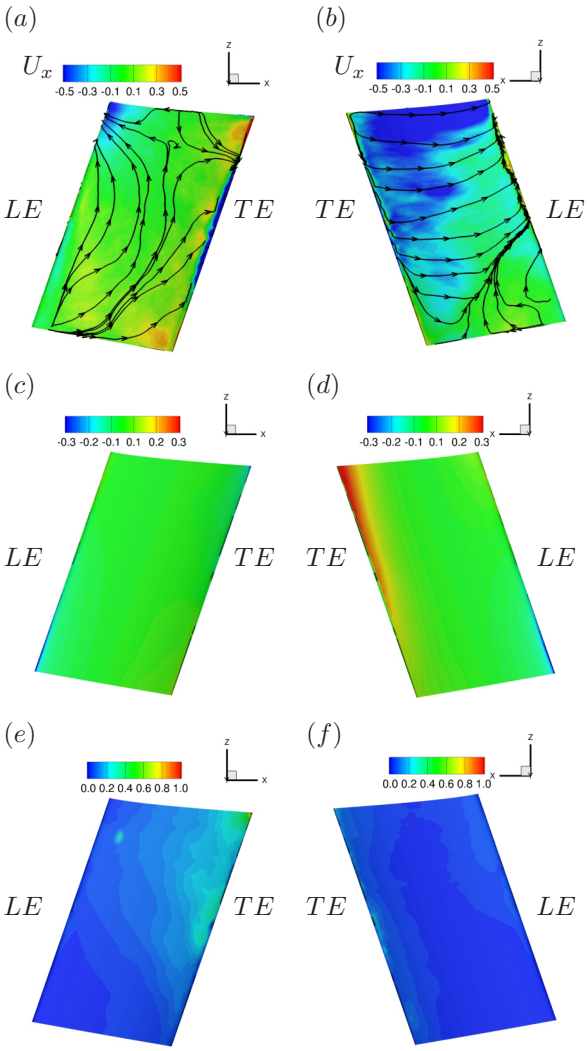

Figure 13: Time averaged flow fields on the stator blades: (a) axial velocity on suction side, (b) axial velocity on pressure side, (c) effective pressure for thrust on suction side, (d) effective pressure for thrust on pressure side, (e) effective pressure for side-force on suction side, (f) effective pressure for side-force on pressure side.

blades in crashback. The previous simulation of Jang & Mahesh (2008) are continued to longer times. The simulation is conducted until 258.7 *revs*, and statistics of the unsteady loads are computed over 128.6 *revs*. Time histories of K_T, K_Q, and K_S are plotted in figure 14. Black solid and blue dashed lines are unsteady loads on blades and duct surfaces, respectively. Jang & Mahesh (2008) significantly overpredicted K_T and K_Q since their computation had transient oscillations. The transient oscillations are absent due to longer computation as shown in figure 14. Mean unsteady loads are given in table 4, which can be compared to experimental results of table 3 and rotor-stator case of table 2. Thrust and torque are still slightly lower than experimental results, but much closer than the previous computational results. The effect of stator blades on thrust and side force is not important, but significantly larger torque is generated on the stator blade surface.

Figure 15 shows circumferentially averaged flow fields for ducted propeller without stator blades, and can be compared to those for ducted propeller with stator blades in figure 11. Axial velocity contours with streamlines and pressure contours are qualitatively similar. The strong reverse flow induced by propeller rotation, tip leakage flow, and high pressure difference between pressure and suction sides are observed in both cases. It indicates that the stator blades do not significantly affect the macro scale flow structure in crashback.

SUMMARY

LES has been performed at an off-design condition of marine propellers, called crashback, which is well

	$\langle K_T \rangle$	$\langle K_Q \rangle$	$\langle K_S \rangle$
LES (blade)	-0.45	-0.087	0.027
LES (duct)	-0.058	0.0013	0.086

Table 4: Unsteady loads for ducted propeller without stator blades from computation.

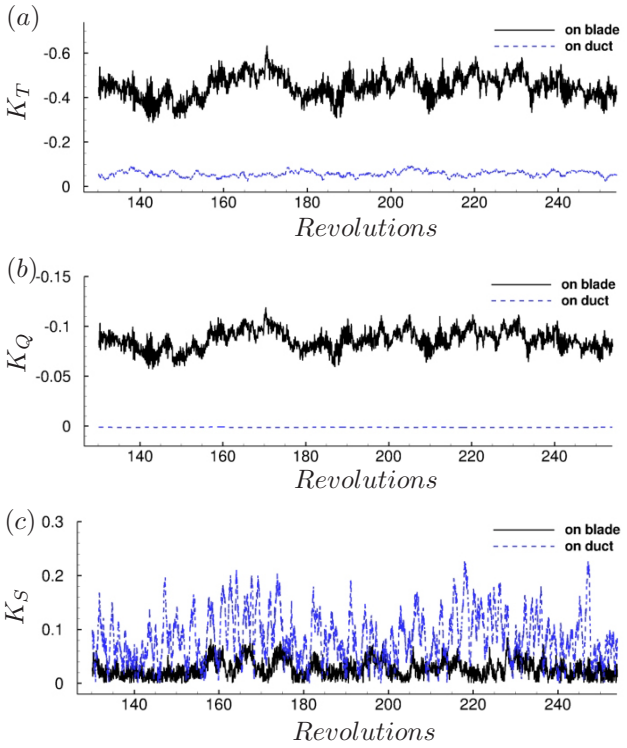

Figure 14: Time histories of unsteady loads on the ducted propeller w/o stators: (a) K_T, (b) K_Q, (c) K_S.

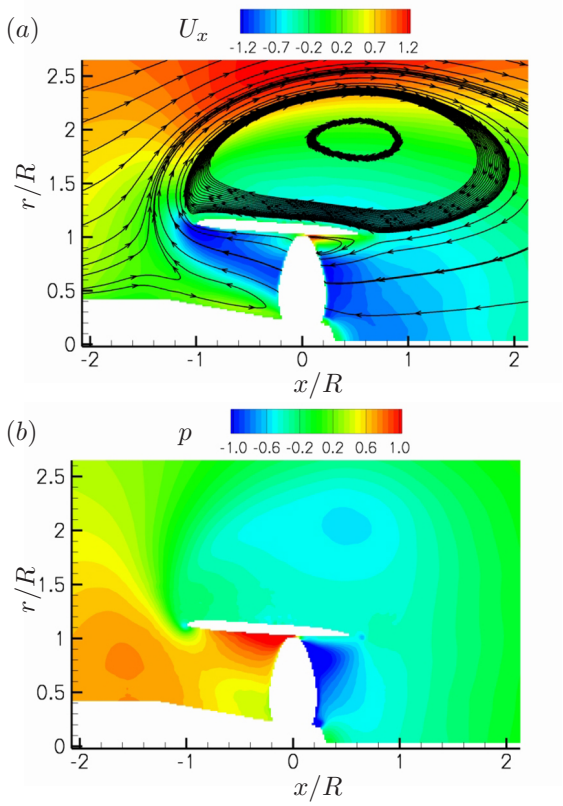

Figure 15: Circumferentially averaged averaged flow fields for ducted propeller w/o stator blades: (a) axial velocity with streamlines, (b) pressure.

known as one of the most challenging operating conditions to analyze. Crashback is characterized by the interaction of the free stream with reverse flow due to reverse propeller rotation. This causes a highly unsteady vortex ring which leads to flow separation and unsteady forces and moments on the blades. The LES uses a discretely kinetic energy conserving algorithm developed by Mahesh *et. al* (2004) for unstructured grids. A sliding interface method is developed to solve the ducted propeller with stator blades. The LES methodology is validated for the open propeller in crashback with the Jessup *et al.* (2004)'s WT experiment, and the sliding interface method is validated in the open propeller case with the rotating frame of reference approach. Computed unsteady loads for the ducted propeller with stator blades are compared to Jessup *et al.* (2006) and Donnelly *et al.* (2008)'s WT results. Thrust and torque are almost the same as the experimental results, and side-force are also in favorable agreement. The effect of the duct on thrust is relatively small, and that on the torque is significantly large. Also, the duct surface is the primary contributor to side-force.

As compared to the open propeller, the flow around ducted propeller in crashback has the following features. Strong reverse flow is found through the propeller disk like the open propeller, but the reverse flow extends along the inner surface of the duct. High forward velocity is observed at the tip gap, which is related to the tip leakage flow. The flow on the outer surface of the duct is almost attached. The pressure difference between the pressure and suction sides is much higher. The physical source of the tip leakage flow is seen to be the large pressure difference between pressure and suction sides. Thrust mostly

arises from the blade surface, but most of side-force is generated from the duct surface. RMS of pressure are much higher on inner surface of duct, especially near blade tips. This implies that side-force on the ducted propeller is caused by the blade-duct interaction, particularly the tip leakage flow.

ACKNOWLEDGEMENTS

This work was supported by the Office of Naval Research under ONR Grant N00014-05-1-0003 with Dr. Ki-Han Kim as program manager. Computing resources were provided by the Arctic Region Supercomputing Center (ARSC) of the High Performance Computing Modernization Program (HPCMP) and the Minnesota Supercomputing Institute (MSI). We are grateful to Dr. Stuart Jessup, Dr. Martin Donnelly, and their colleagues at NSWCCD for providing us with experimental data.

REFERENCES

Blades, E. L., Marcum, D. L., "A Sliding Interface Method for Unsteady Unstructured Flow Simulations," *Int. J. Numer. Meth. Fluids*, **53**, 507-529, (2007).

Bridges, D. H., Donnelly, M. J., Park, T. J., "Experimental investigaton of the submarine crashback maneuver," *Journal of Fluids Engineering*, **130**, (2008).

Chang, P., Ebert, M., Young, Y.L., Liu, Z., Mahesh, K., Jang, H., Shearer, M., "Propeller forces and structural responses to crashback," *Proceedings of the 27^{th} Symposium on Naval Hydrodynamics*, Seoul, Korea, (2008)

Chen, B., Stern, F., "Computational Fluid Dynamics of Four Quadrant Marine Propeller Flow," *Journal of Ship Research*, **43:4**, 218, (1999).

Donea, J., Huerta, A., Ponthot, J.-Ph., Rodriguez-Ferran, A., "Arbitrary Lagrangian-Eulerian Methods," *The Encyclopedia of Computational Mechanics*, Wiley, Vol. 1, Chap. 14, (2004).

Donnelly, M., Jessup, S., Etebari, A., "Measurement of Steady and Unsteady Duct Loads for Propeller 4381 at Crashback Conditions in the 36 in. Water Tunnel," *Hydromechanics Department Report*, Naval Surface Warfare Center, NSWCCD-50-TR-2008, (2008).

Germano, M., Piomelli, U., Moin, P., Cabot, W. H., "A dynamic Subgrid-Scale Eddy Viscosity Model," *Physics of Fluids A*, **3:7**, 1760, (1991).

Hecker, R., Remmers, K., "Four quadrant open-water performance of propellers 3710, 4024, 4086, 4381, 4382, 4383, 4384 and 4426," *David Taylor Naval Ship Research and Development Center*, Report NSRADC 417-H01, (1971).

Jang, H., Mahesh K., "Large Eddy Simulation of Ducted Propulsors in Crashback," *Proceedings of the 27^{th} Symposium on Naval Hydrodynamics*, Seoul, Korea, (2008).

Jang, H., Mahesh K., "Large Eddy Simulation of Marine Propellers in Crashback," *Proceedings of the 28^{th} Symposium on Naval Hydrodynamics*, Pasadena, California, (2010).

Jang, H., Mahesh K., "Large Eddy Simulation of Flow arond a Reverse Rotating Propeller," *Submitted to Journal of Fluid Mechanics*, (2012).

Jessup, S., Chesnakas, C., Fry, D., Donnelly, M., Black, S., Park, J., "Propeller Performance at Extreme Off Design Conditions," *Proceedings of the 25^{th} Symposium on Naval Hydrodynamics*, St. John's, Canada, (2004).

Jessup, S., Fry, D., Donnelly, M., "Unsteady Propeller Performance in Crashback Conditions With and Without Duct," *Proceedings of the 26^{th} Symposium on Naval Hydrodynamics*, Rome, Italy, (2006).

Jiang, C. W., Dong, R. R., Lui, H. L., Chang, M. S., "24-inch Water Tunnel Flow Field Measurements During Propeller Crashback," *21^{st} Symposium on Naval Hydrodynamics*, The National Academies Press, Washington DC, 136, (1997).

Karypis, G., and Kumar, V., "Multilevel Algorithms for Multi-Constraint Graph Partitioning, Technical Report TR 98-019," Department of Computer Science, University of Minnesota, Minneapolis, MN, 1998.

Lilly, D. K., "A Proposed Modification of the Germano Subgrid-Scale Closure Model," *Physics of Fluids A*, **4:3**, 633, (1992).

MacPherson, I., Rodgers, J, R., Allen, C. B., Fenwick, C. L., "Sliding and Non-Matching Grid Methods for Helicopter Simulations," *AIAA Paper* No. 2006-1070, (2006).

Mahesh, K., Constantinescu, G., Moin, P., "A Numerical Method for Large-Eddy Simulation in Complex Geometries," *Journal of Computational Physics*, **197:1**, 215, (2004).

Pan, D., Chao, M. J., and Chien, S. K., "Euler Computations of Rotor Flows on Unstructured Rotating Meshes," *Journal of Aircraft*, **38:4**, 672-679, (2001).

Steijl, R., Barakos, G., "Sliding Mesh Algorithm for CFD Analysis of Helicopter Rotor-Fuselage Aerody-

namics," *Int. J. Numer. Meth. Fluids*, **58**, 527-549, (2008).

Verma, A., Jang, H., Mahesh, K., "Large Eddy Simulation of the Effect of Hull on Marine Propulsors in Crashback," *Second International Symposium on Marine Propulsors*, Hamburg, Germany, (2011).

Verma, A., Jang, H., Mahesh, K., "Large Eddy Simulation of Flow around a Reverse Rotating Propeller," *Submitted to Journal of Fluid Mechanics*, (2012).

Vyšohlid, M., Mahesh, K., "Large Eddy Simulation of Crashback in Marine Propellers," *Proceedings of the 26^{th} Symposium on Naval Hydrodynamics*, Rome, Italy, (2006).

Vyšohlid, M., Mahesh, K., "Understanding Crashback in Marine Propellers Using an Unsteady Actuator Disk Model," *45^{th} AIAA Aerospace Sciences Meeting and Exhibit*, Reno, Nevada, (2007).